Influence of fluids on earthquakes based on numerical modeling

MARGUIN Valentin[1] and Simpson Guy[1]

[1]University of Geneva

November 25, 2022

Abstract

The strength and sliding behavior of faults in the crust is largely controlled by friction and effective stress, which is itself modulated by fluid pressure. Most earthquake models assume a fixed pore fluid pressure despite widespread evidence that is varies strongly in time due to changes in permeability. Here we explore how dynamic changes in pore pressure influence the properties of earthquakes in the upper crust. To study this problem we develop a two dimensional model that incorporates slow tectonic loading and fluid pressure generation during the interseismic period with frictional sliding on a thrust fault whose permeability evolves with slip. We find that the presence of relatively modest fluid overpressures tends to reduce coseismic slip, stress drop, maximum sliding velocity, rupture velocity and the earthquake recurrence time compared to models without fluids. Our model produces a wide range of sliding velocities from rapid to slow earthquakes, which occur due to the presence of high pore pressures prior to rupture. The models also show evidence for aftershocks that are driven by fluid transfer along the fault plane after the mainshock. Overall, this study shows that fluids can exert an important influence on earthquakes in the crust, which is mostly due to modulation of the effective stress and variations in permeability, and to a lesser extent to poro-elastic coupling.

Influence of fluids on earthquakes based on numerical modeling

MARGUIN Valentin, SIMPSON Guy

University of Geneva, Department of Earth Sciences

Key Points:

- Properties of earthquakes are markedly influenced by the presence of fluid overpressures.
- Ruptures in wet models have relatively low stress drops, sliding speed and rupture velocity.
- Slow slip events and aftershocks might be a fingerprint of fluid overpressures.

Corresponding author: Marguin Valentin, `valentin.marguin@unige.ch`

Abstract

The strength and sliding behavior of faults in the crust is largely controlled by friction and effective stress, which is itself modulated by fluid pressure. Most earthquake models assume a fixed pore fluid pressure despite widespread evidence that is varies strongly in time due to changes in permeability. Here we explore how dynamic changes in pore pressure influence the properties of earthquakes in the upper crust. To study this problem we develop a two dimensional model that incorporates slow tectonic loading and fluid pressure generation during the interseismic period with frictional sliding on a thrust fault whose permeability evolves with slip. We find that the presence of relatively modest fluid overpressures tends to reduce coseismic slip, stress drop, maximum sliding velocity, rupture velocity and the earthquake recurrence time compared to models without fluids. Our model produces a wide range of sliding velocities from rapid to slow earthquakes, which occur due to the presence of high pore pressures prior to rupture. The models also show evidence for aftershocks that are driven by fluid transfer along the fault plane after the mainshock. Overall, this study shows that fluids can exert an important influence on earthquakes in the crust, which is mostly due to modulation of the effective stress and variations in permeability, and to a lesser extent to poro-elastic coupling.

Plain Language Summary

In this study we use a numerical model to investigate how fluid pressures vary over the seismic cycle and how they interact with and influence the properties of earthquakes that occur in the upper crust. In the model, fluid overpressures are generated slowly during the interseismic period by phenomena such as dehydration reactions while they are episolidically released during earthquakes due to fracturing and a dramatic increase in permeability. The models show that the presence of high fluid pressures has an important influence on earthquakes. High fluid pressures favor smaller, more frequent earthquakes. Also high fluid pressures may sometimes be responsible for aftershocks and for anomalously slow earthquakes that involve slip over several months rather than several seconds. Overall, we show that the presence of fluids in the crust plays an integral part in the earthquake process.

1 Introduction

Understanding the physical parameters that modulate seismicity and that control the properties of earthquakes remains an ongoing challenge in earthquake mechanics. Several factors play a key role, one of which is the fault strength, which in the upper crust is determined by the product of the friction coefficient and the effective normal stress (i.e., the total normal stress minus fluid pressure). Much attention has been focused on how fault strength varies due to changes in the friction coefficient during sliding (Dieterich, 1978; Ruina, 1983; Marone, 1998; Scholz, 1998). Changes in friction are quite subtle at relatively low sliding velocities (i.e., <1 mm/s) (Dieterich, 1978; Ruina, 1983), but they may become profound at slip rates similar to those typically encountered during fast earthquakes (Tsutsumi & Shimamoto, 1997; Di Toro et al., 2004; Goldsby & Tullis, 2011). These results provide a basis for understanding why some faults appear to be anomalously weak (Scholz, 2006). However, most earthquake stress drops are between 1-10 MPa (Abercrombie & Rice, 2005; Allmann & Shearer, 2009), which suggests that shear stress levels must also be low prior to rupture (Noda et al., 2009, 2011). One way this might be achieved is with elevated pore pressures, which would reduce the effective normal stress, and thus enable faults to rupture at relatively low shear stresses (Simpson, 2018).

There are a number of mechanisms that could act to increase fluid pressures during the interseismic period at depths where earthquakes are typically nucleated ($\sim$ 10 km) (Osborne & Swarbrick, 1998). For example, fluids are being continuously released from dehydration reactions (Connolly, 1997; Leclère et al., 2018) and cooling magmas at these and greater depths (Hedenquist & Lowenstern, 1994; Weis et al., 2012), which owing to their low density, rise toward the surface. Concomitantly with this, compaction (viscous or elastic) closes pores and cracks and reduces permeability, thereby hindering the escape of fluids and increasing the fluid pressure (Walder & Nur, 1984). Numerous studies have provided evidence to suggest that fluid pressures in the crust are elevated, sometimes approaching the lithostatic pressure (Etheridge et al., 1984; Fisher et al., 1995; Suppe, 2014; Sibson, 2017).

The build up of fluid overpressure in the upper crust is counteracted by the onset of brittle fracture and/or frictional sliding on preexisting faults due to dilatancy and permeability enhancement that enable excess pore pressures to dissipate (Sibson, 1990; Miller & Nur, 2000). Substantial evidence shows that faults transiently act as major fluid conduits and that this is associated with rapid and dramatic drops in fluid pressure (Sibson et al., 1988; Cox, 2005). Fault rocks are typically highly fractured and cemented, which suggests that the permeability repeatedly cycles between high and low values (Chester & Logan, 1986; Cox & Munroe, 2016). Collectively, these observations have lead to the notion that some major faults act at pressure values, sporadically slipping and releasing fluid overpressures before resealing and enabling shear stresses and fluid overpressures to be reestablished (Sibson, 1990, 1992; Cox, 2005).

Despite the wealth of field evidence supporting the concept of fault-value behaviour, it is noteworthy that most earthquake models do not explicitly account for variations in fluid pressure with sliding. Many models assume a highly overpressured fault, a requirement that is necessary in order to obtain realistic stress drops and slip behaviour (Lapusta & Rice, 2003; Liu et al., 2005). However, if permeabilities on a fault increase dramatically during sliding as evidence suggests (Sibson et al., 1988; Cox, 2005), then the fluid pressure is likely to change rapidly during an earthquake, which could potentially impact on rupture dynamics. Various workers have studied different aspects of fault-value behaviour using modeling and have shown that fluids might be responsible for aftershocks, transient creep, seismic swarms, and in general, smaller seismic events (Sleep & Blanpied, 1992; Miller et al., 2004; Acosta et al., 2018; Petrini et al., 2020; Zhu et al., 2020)

In this work we focus on how earthquakes are modulated by long term generation of fluid overpressures during the interseismic period coupled with rapid changes in fluid pressure caused by a sharp increase in the fault permeability during rupture. This is achieved by studying a two dimensional mechanical model based on sliding on a thrust fault governed by rate- and state-dependent friction (Dieterich, 1978; Ruina, 1983) coupled to poro-viscoelastic deformation and fluid flow in the surrounding crust. Our model shares some similarities with the study of Zhu et al., (2020) except that we incorporate full poro-elasticity, 2D fluid flow (i.e., on and off-fault) and more dramatic coseismic variations in permeability. Although the model presented is generic and not applied to any specific case, the setup and parameters are chosen to be representative of a continental convergent plate boundary setting.

2 Governing equations

We simulate ruptures on a preexisting 30° dipping reverse fault embedded within a 15 km thick poro-elastic layer that overlies a 15 km thick poro-viscoelastic substrate (Figure 1a). The entire domain is pushed laterally over a rigid base at 25 mm/year. The upper boundary is a free surface. Model parameters are summarized in Table 1.

Deformation of the porous solid is governed by combining force balance with the constitutive relations for a viscoelastic material. Assuming quasi-static conditions, the two dimensional force balance equation can be written as

$$\nabla^T \left(\sigma' - \alpha\, m\, P_f\right) = -[0, 0, -\rho\, g]^T \tag{1}$$

where ∇ is the gradient operator, σ' is the effective stress vector (using Voigt notation), α is Biot's coefficient, m is the vector form of kronecker's delta (δ_{ij}), P_f is fluid pressure, ρ is rock density, and g is acceleration due to gravity.

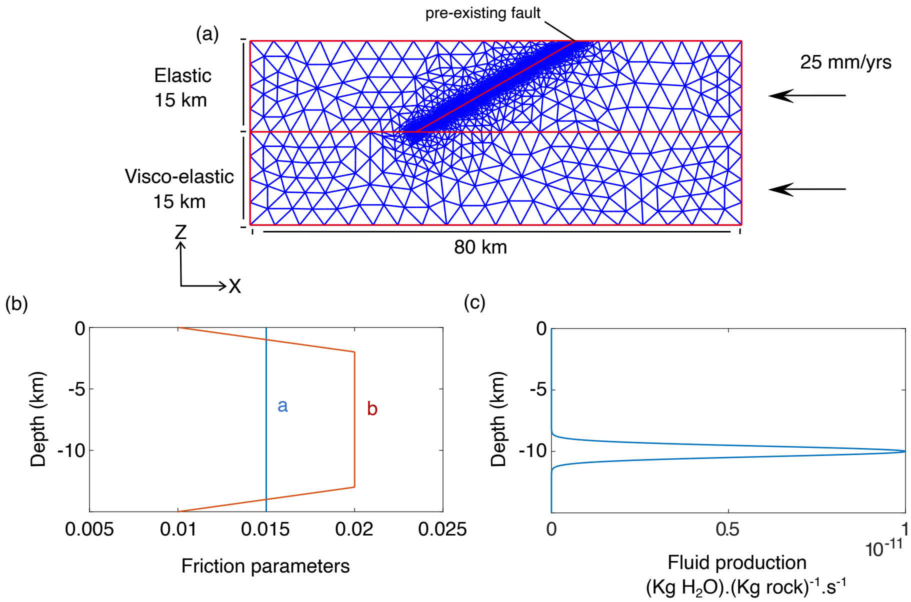

Figure 1. (a). Typical FEM model setup for 2D simulation [(Simpson, 2018)], (b). Rate and state friction parameters in the upper elastic layer (see equation 7), (c). Fluid production rate in model with $S_0 = 10^{-11}$ (kg H_2O) (kg rock)$^{-1}$ s^{-1} (see equations 5 and 12).

The stress-strain relation for an isotropic Maxwell viscoelastic material can be written as

$$\frac{\partial \sigma'}{\partial t} = D \, \frac{\partial \epsilon}{\partial t} + D_0 \, \sigma' \tag{2}$$

where D and D_0 are viscoelastic material matrices and ϵ is the strain vector. The kinematic relation between strains and velocities (assuming small strains) can be written as

$$\frac{\partial \epsilon}{dt} = \nabla \, V \tag{3}$$

where V the velocity vector ($V = V_f + V_s$; V_f=fault velocity; V_s=solid velocity). Combining the last two equations (i.e., equation 2 and 3), gives

$$\frac{\partial \sigma'}{\partial t} = D \, \nabla_s V + D_0 \, \sigma' \tag{4}$$

We discretise this equation using a forward Euler finite difference approximation and substitute it into 1 to leave a system of equations with velocities and fluid pressure as the unknowns.

The equation governing fluid pressure in obtained by combining mass balance of the fluid with Darcy's law. This equation can be written as

$$\phi \, \beta \, \frac{\partial P_e}{\partial t} = \nabla . \left(\frac{k}{\eta_f} \, \nabla P_e \right) - \alpha \, m^T \, \nabla \, V + S \tag{5}$$

where P_e the fluid pressure in excess of hydrostatic (i.e., $P_e = P_f - \rho_f g z$), ϕ is the porosity (taken as a constant), β is the bulk compressibility, k the permeability (considered to vary as a function of sliding rate and effective stress, as outlined below), η_f is the viscosity of the fluid, α is Biot's coefficient, V are the velocities of the solid and S is a fluid pressure source term (with units (kg H_2O)/((kg rock)/s) that varies of a function of space (see below). This equation states that variations in fluid pressures occur in response to three effects:

porous flow (term 1 on the right hand side of equation 5), volumetric deformation of the poro-viscoelastic solid (term 2) and fluid production (term 3).

Sliding on the fault is governed by Coulomb's criterion combined with rate- and state-dependent friction. Coulomb's condition can be written as

$$\tau = f(V_f, \theta)\, \sigma_n' \tag{6}$$

where τ is the shear stress, σ_n' is the effective normal stress, and $f(V_f, \theta)$ is the friction coefficient that is given by (Dieterich, 1979; Ruina, 1983; Marone, 1998)

$$f(V_f, \theta) = f_o + a \ln\left(\frac{V_f}{V_o}\right) + b \ln\left(\frac{\theta}{\theta_o}\right) \tag{7}$$

In this equation f_o is the friction coefficient at a reference sliding rate V_0, V_f is the sliding velocity, a is a dimensionless friction parameter measuring the strength of the direct velocity dependency, b is a dimensionless coefficient measuring the strength of the state dependence (see Fig.1b), θ is a state variable (that can be interpreted as the average age of an asperity on the fault) and θ_0 is the state variable at V_0. In this work we use the aging law for evolution of the state (Dieterich, 1979):

$$\frac{\partial \theta}{\partial t} = 1 - \frac{V_f \theta}{d_c} \tag{8}$$

where d_c is the state evolution distance. Our approach to solve for the sliding rate on the fault is as follows: (1) solve the equations governing deformation of the poro-viscoelastic solid for the shear stress on the fault (see equation 4), (2) reduce this shear stress by subtracting the term ΩV_f to account for radiation damping (where $\Omega = \mu/2c_s$, where μ is the shear modulus and c_s is the shear wave speed), (3) set the result to the Coulomb condition (see Equation 6) and (4) solve for the fault slip rate V_f.

The permeability is an an important but poorly constrained variable, varying by at least 10 orders of magnitude under upper crustal conditions (Manning & Ingebritsen, 1999). Experiments have shown that permeability depends strongly on the effective confining pressure due to elastic closure of cracks and pores (Brace et al., 1968; Rice, 1992; Evans et al., 1997). Here, we assume that this can be described by the relation (Rice, 1992)

$$k_p = k_{min} + (k_0 - k_{min}) \exp\left(\frac{\bar{\sigma}'}{\sigma *}\right) \tag{9}$$

where k_p is the pressure-dependent permeability, k_0 the permeability when the mean effective stress is null, k_{min} is the minimum background permeability, $\bar{\sigma}'$ is the mean effective stress (negative in compression) and $\sigma*$ is a parameter measuring the sensitivity of permeability to the effective confining pressure. Experiments show that $\bar{\sigma}*$ is equal to 30 MPa (typically of the order of 10 MPa (Brace et al., 1968; Evans et al., 1997)). The fault permeability is also known to change drastically over the duration of the seismic cycle (Miller, 1997). Rapid sliding during an earthquake can produce an extremely high permeability due to fracturing and dilatancy (Sibson, 1986; Cox & Munroe, 2016; Im et al., 2019) whereas after an earthquake compaction and mineral precipitation act to reduce permeability (Renard et al., 2000; Tenthorey et al., 2003). We capture these mechanisms using the following heuristic evolution equations

$$\begin{aligned} \frac{\partial k_f}{\partial t} &= \frac{k_{max} - k_f}{T_S} \quad \text{if } V_f \geq V_c \\ \frac{\partial k_f}{\partial t} &= \frac{k_{min} - k_f}{T_H} \quad \text{if } V_f < V_c \end{aligned} \tag{10}$$

where k_f is the permeability on the fault, k_{max} corresponds to the maximum fault permeability during an earthquake, k_{min} is the minimum permeability, V_f the fault velocity, V_c is a critical sliding velocity and T_S and T_H are characteristic time scales for the permeability to increase (due to sliding during an earthquake) and decrease (by healing), respectively.

The first equation accounts for an increase in permeability once the slip rate exceeds V_c, while the second equation describes the exponential decay of permeability once rapid sliding has terminated (see figure 2). The parameters appearing in these equations are poorly constrained owing to the complexity of the governing processes and the difficulty of obtaining measurements at the relevant spatial and temporal scales. The maximum permeability could be very high, similar to that of a highly porous sediment such as a gravel if the fault rocks become highly fractured and porous. In our simulations we investigate a range of values extending from 10^{-8} to 10^{-9} m^2. The minimum permeability could be very low, similar to a granite or low porosity limestone. Here we assume that $k_{min} = 10^{-19}$ m^2 (Selvadurai et al., 2005). For the evolution time scales, we take 1 s for T_S and 2 years for T_H. This latter value is within the range suggested by healing observed on natural faults (Xue et al., 2013). We take 1 mm/s for the critical sliding velocity (V_c) that controls the transition between a permeability increase and decrease. The total permeability is computed as

$$k = k_p + k_f. \tag{11}$$

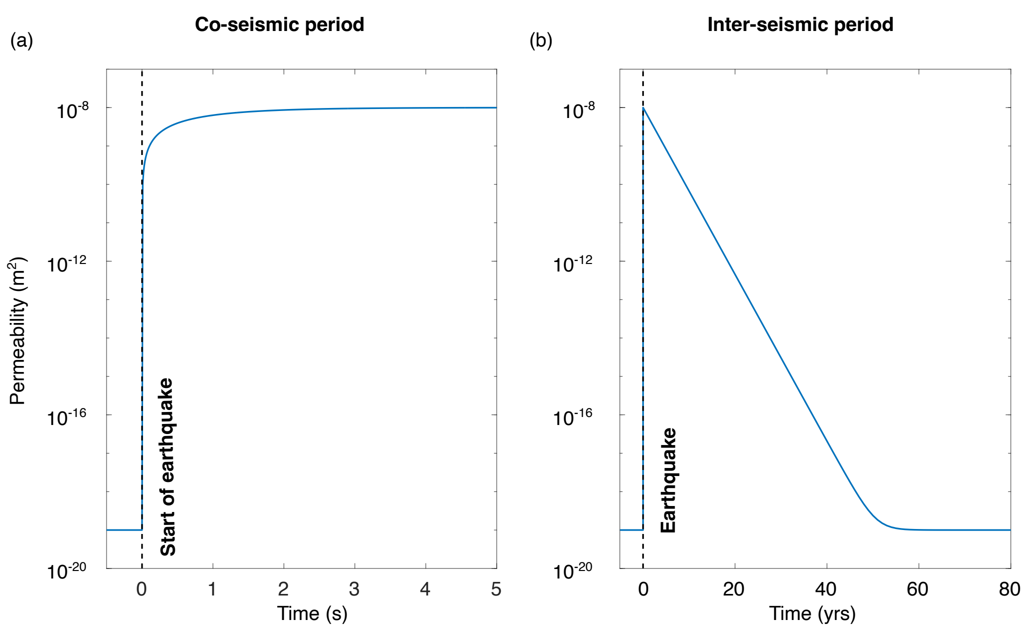

Figure 2. Illustration of permeability evolution (see equation 10) on the fault during (a) coseismic period (when $V_f > V_c$) and (b) postseismic-interseismic period (when $V_f < V_c$). In this example, k_{min}=10^{-19} m^2, $k_{max} = 10^{-8}$ m^{-2}, T_S=1 s and T_H=2 yrs.

Fluid overpressures are introduced into the model by considering a horizontal fluid source within the upper seimogenic layer (see equation 5), which is crudely intended to mimic fluid release from a dehydration reaction. The devolatisation rate for a metamorphic dehydration reaction depends on a variety of factors including the Gibbs energy (involving temperature and pressure), the stoichometry of the specific reaction and the surface area of the rate limiting mineral (Connolly, 1997). Here we avoid these complexities and use a simple parametrization assuming a Gaussian function (see figure 1c)

$$S = S_0 \exp\left(\frac{-(z - z_0)^2}{2\gamma^2}\right) \tag{12}$$

where z the depth, z_o the depth where the production rate is the greatest, S_0 the maximum fluid production rate ((kg H_2O)/(kg rock)/s), and γ is a length scale controlling the full width at half maximum (H) of the band ($H \approx 2.355\gamma$). In our simulations the fluid production layer is centered at 10 km depth and is approximately 2 km across (from top to bottom).

Table 1. Model parameters

Parameter	Symbol	Value
Domain dimension	D_z, D_x	30 km, 80 km
Fault dip		30°
Boundary velocity	V_B	25 mm/yr
Shear modulus	μ	30 GPa
Shear wave speed	c_s	
Viscosity of upper layer	η_{UC}	10^{32} Pa.s
Viscosity of lower layer	η_{LC}	10^{19} Pa.s
Gravity	g	9.81 m/s^2
Rock density	ρ	2700 kg/m^3
Fluid density	ρ_f	1000 kg/m^3
Porosity	ϕ	0.1
Biot's coefficient	α	1
Fluid viscosity	η_f	1.83.10^{-4} Pa.s
Bulk compressibility	β	5.10^{-10} Pa^{-1}
Fluid source parameter	Z_0	10 km
Fluid Source parameter	H	1000 m
Fluid source parameter	S_0	10^{-10} - 10^{-13} (kg H_20) (kg rock)$^{-1}$ s^{-1}
Permeability parameter	$\sigma*$	30 MPa
Healing time scale	T_H	2 yrs
Sliding time scale	T_S	1 s
Maximum fault permeability	k_{max}	10^{-8} - 10^{-9} m^2
Minimum rock permeability	k_{min}	10^{-19} m^2
Permeability parameter	k_0	10^{-12} m^2
Critical sliding velocity	V_c	10^{-3} m/s
Direct effect parameter	a	0.015
State evolution parameter	b	see Fig.1b
State evolution distance	d_c	0.025 m
Reference velocity	V_0	10^{-6} m/s
Reference friction coefficient	f_0	0.6
Radiation damping term	Ω	5 MPa.s/m

The above system of partial differential equations is solved for velocities and fluid pressure using the continuous Galerkin Finite Element method employing 7-node triangles and 7 integration points (Simpson, 2017) . We use an unstructured mesh that permits local refinement adjacent to the fault, where a typical element size is ∼40 m. Adaptive time stepping is used to transition between the interseismic period (where time steps are on the order of 1 year) and times when rupture is taking place, when time steps are on the order of 1 μs (but which decrease with increasing sliding velocity).

3 Results

Two main classes of simulations have been performed. A 'dry' simulation was performed by setting the fluid pressure source to zero (i.e., $S = 0$ in equation 5) and by constraining the permeability to a uniformly high value ($k = 10^{-8}$ m^2) to avoid any fluid overpressure. Thus, the fluid pressure in the dry model remains hydrostatic throughout the simulation.

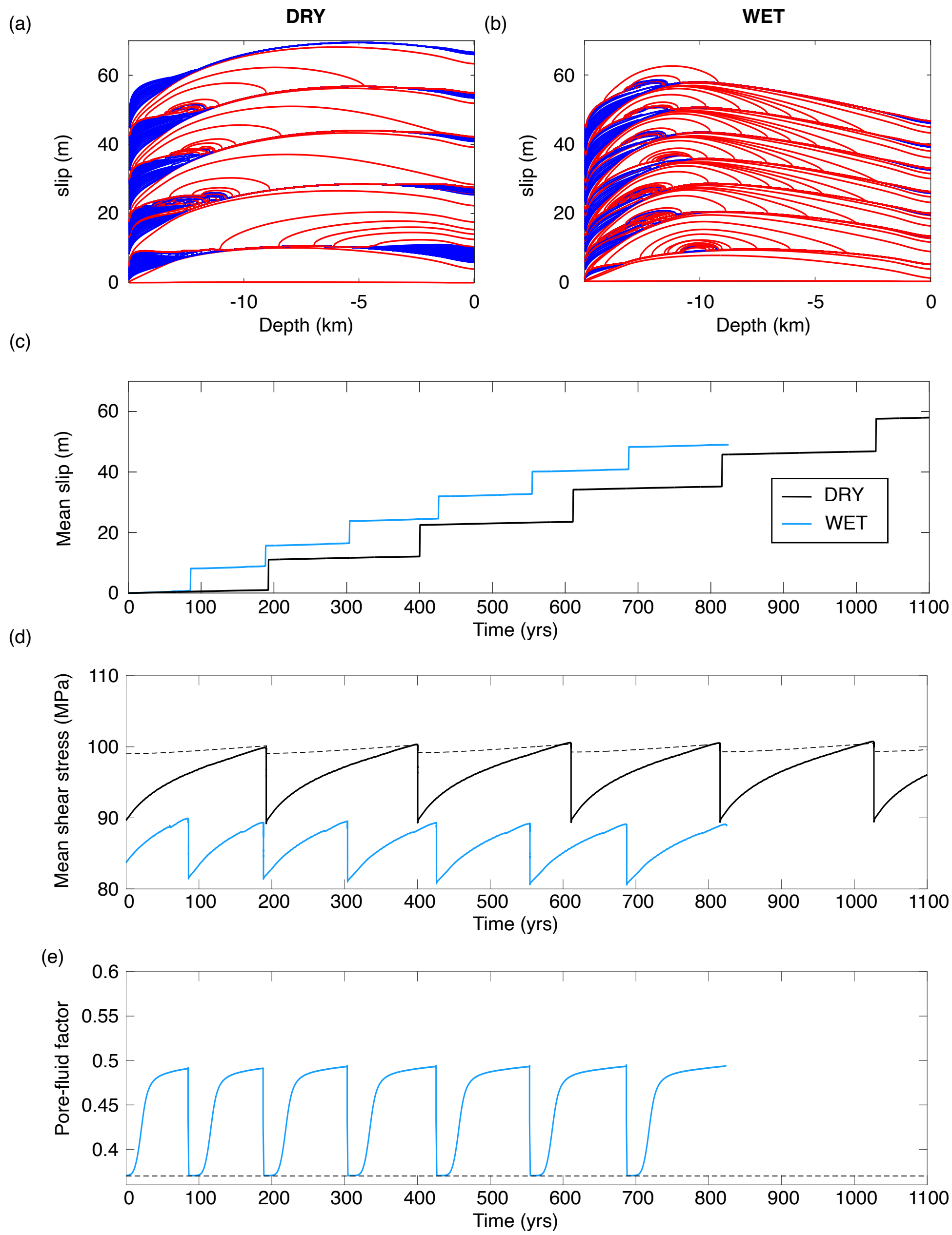

Figure 3. Computed rupture sequence on a reverse fault for "dry" (a) and "wet" (b) models ($S_0 = 10^{-11}$ s^{-1} and $K_{max} = 10^{-8}$ m^2). Slip contours are plotted every 5 seconds during the coseismic period (red) and every 5 years during the interseismic period (blue). (c) Mean slip (m) as a function of time (yrs) for 2 simulations: "dry" (black curve), "wet" with fluid source (blue curve). (d). Mean shear stress $\overline{\tau}$ versus time for the "dry" model (black curve) and the "wet" model (blue curve). The black dashed line shows the frictional strength assuming constant friction (0.6) and a hydrostatic fluid pressure. (e) Pore fluid factor λ for "wet" model versus time (blue curve), at the maximum fluid production depth (i.e, 10 km depth). Black dotted line shows the pore fluid factor for a hydrostatic fluid pressure.

This is compared to 'wet' simulations that include fluid production and lower background permeabilities, together which lead to the generation of fluid overpressures. Results for a dry and wet simulation are compared in Figure 3. For the dry case, one sees a series of large earthquakes (red curves) that nucleate close to the base of the elastic layer and that rupture into the overlying poro-elastic medium (Figure 3a). These are separated by periods when slip is dominated by slow creep (blue curves) at the base of the fault and close to the surface. The wet simulation shows a similar rupture sequence (Figure 3b) but it differs from the results of the dry model in several respects. First, in the wet model coseismic slip is smaller and the recurrence time is shorter (both by about 50%) compared to the dry model (Figure 3c). Second, in the dry model, the ruptures grow as expanding cracks whereas in the wet model, they are more pulse-like (cf Figures 3a and b). Third, for the dry model, earthquakes are nucleated at the base of the fault near the transition from velocity strengthening to velocity weakening behaviour (which occurs at 14 km depth, see Figure 1b). In the wet model, earthquakes are consistently nucleated at shallower depths, closer to the level where fluid production (and hence fluid overpressure) is at its greatest (i.e., 10 km).

The differences in the rupture sequences between dry and wet models are directly related the control of fluid pressures on the effective normal stress, and therefore to the shear stress on the fault at rupture. In the dry models, the shear stress is relatively elevated ($\overline{\tau}$ approximately 100 MPa) because the fluid pressure is constantly low (Figure 3d and e). In the wet simulation, the pore fluid ratio ($\lambda = P_f/\sigma_z$) at the maximal fluid production depth (i.e. 10 km depth) oscillates between 0.37 (corresponding to a hydrostatic fluid pressure) immediately after an earthquake and ~ 0.5 just prior to rupture (corresponding to a fluid overpressure of approximately 35 MPa), which enables the fault to slide at lower shear stress ($\overline{\tau}$ approximately 90 MPa). It also accounts for the lower stress drops and changes in how the wet ruptures propagate (i.e pulse-like mode (Zheng & Rice, 1998)).

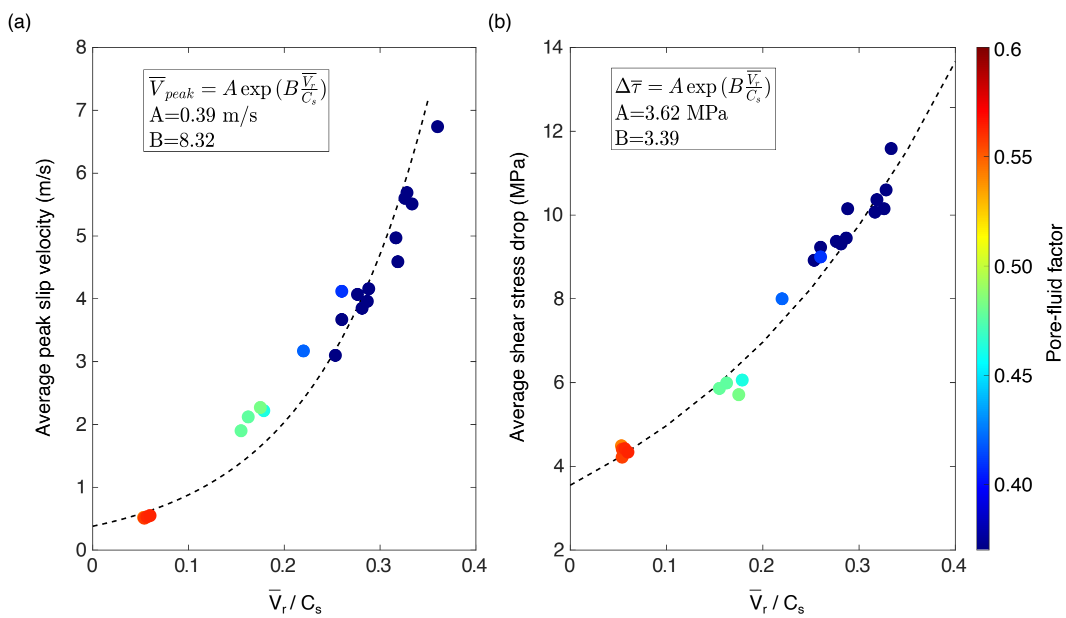

Figure 4. (a). Average peak sliding velocity ($\overline{V}_{peak}$) as a function of the ratio between the average rupture velocity ($\overline{V}_r$) and the shear wave speed (C_s). (b) Average shear stress drop ($\Delta\overline{\tau}$) as a function of the average rupture velocity over the shear wave velocity. Colorbar represents the pore fluid factor λ (at the onset of fault slip), defined as the ratio of the fluid pressure to the vertical stress. We have taken the mean rupture velocity in the middle of the fault to avoid edge effects.

We have performed a variety of simulations with different fluid source magnitudes (i.e, varying S in equation 5) in order to investigate the dependency of fluid pressure on rupture properties. The results show that the average peak sliding velocity, rupture speed and shear stress drop all decrease systematically with the magnitude of fluid overpressure at the onset of rupture (Figure 4). In addition, we observe that both the peak siding velocity and the stress drop increase with increasing rupture velocity, as observed in other studies (Bizzarri, 2012; Passelègue et al., 2020). In all cases, we observed rupture velocities well below the shear wave speed.

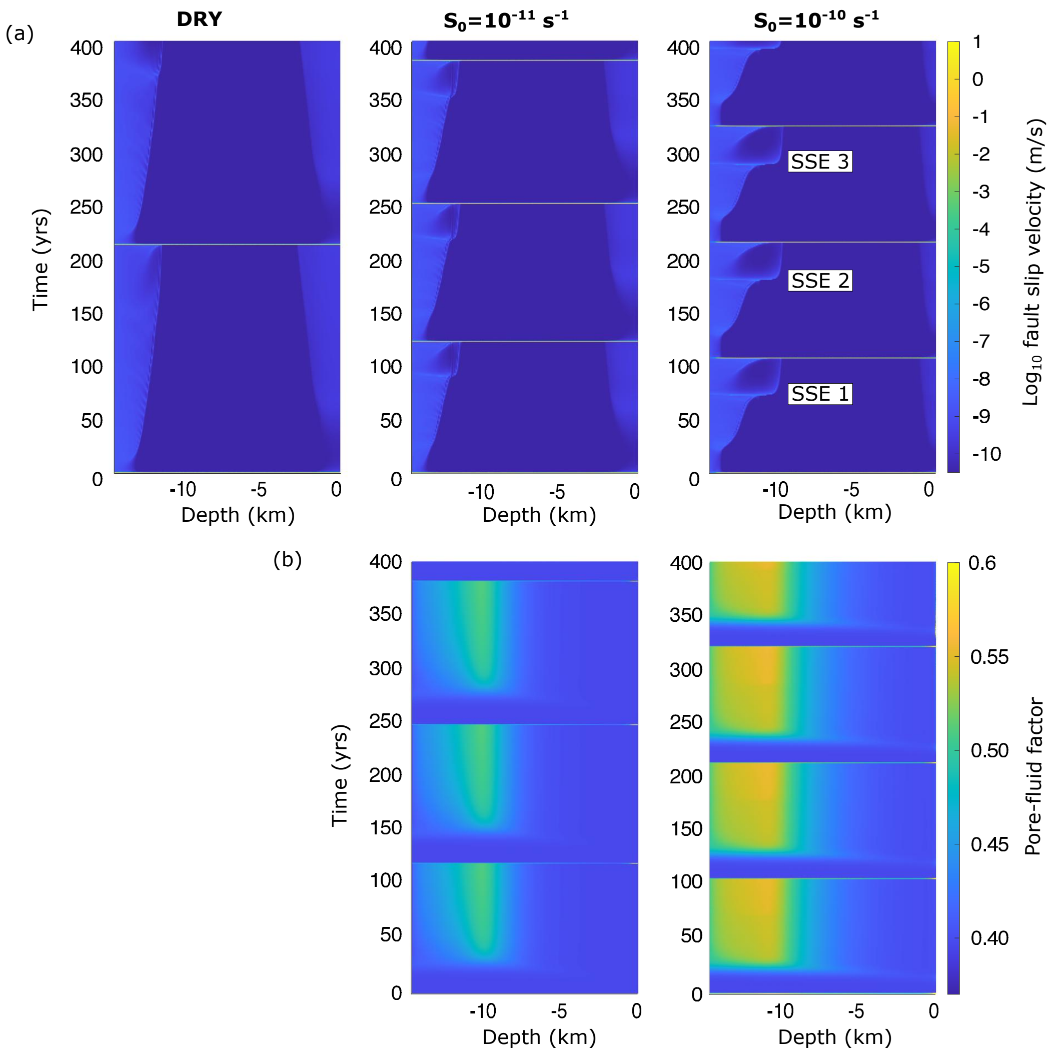

Figure 5. Time depth plots for a "dry" and two "wet" simulations showing the sliding velocity (a) and pore pressure ratio on the fault (b). The simulation with the highest rate of fluid production ($S_0 = 10^{-10}$ s^{-1}) shows distinct slow slip events (labeled SSE 1, SSE 2 and SSE 3) in the periods between mainshocks.

In simulations with relatively high rates of interseismic fluid production ($S_0 > 10^{-10}$ s^{-1}) we observe a series of slow slip events (SSE's) in the intervals between normal 'fast' earthquakes (Figure 5). The slow slip events in our simulations have peak sliding velocities of $\sim 10^{-7}$ m/s, rupture durations of ~ 1 year and they produce horizontal displacements at the surface directly above the rupture zone of about 3 cm (Figure 6). Slow slip events are not observed when fluid production rates are lower than $S_0 < 10^{-11}$ s^{-1}. In this case, interseismic creep occurs only on the lower, frictionally-stable portion of the fault ($\leq$ -12 km depth). For higher fluid production rates, creep can extend to lower depths where it becomes increasingly rapid because it encounters progressively higher fluid pressures linked to the fluid source at 10 km. These events eventually arrest as they pass through the source zone (i.e., to shallower depths) where fluid overpressures are lower. We note that the pore pressure ratio at the onset of the SSE's in Figure 5b is approximately 0.6, indicating fluid pressures well below the lithostatic pressure.

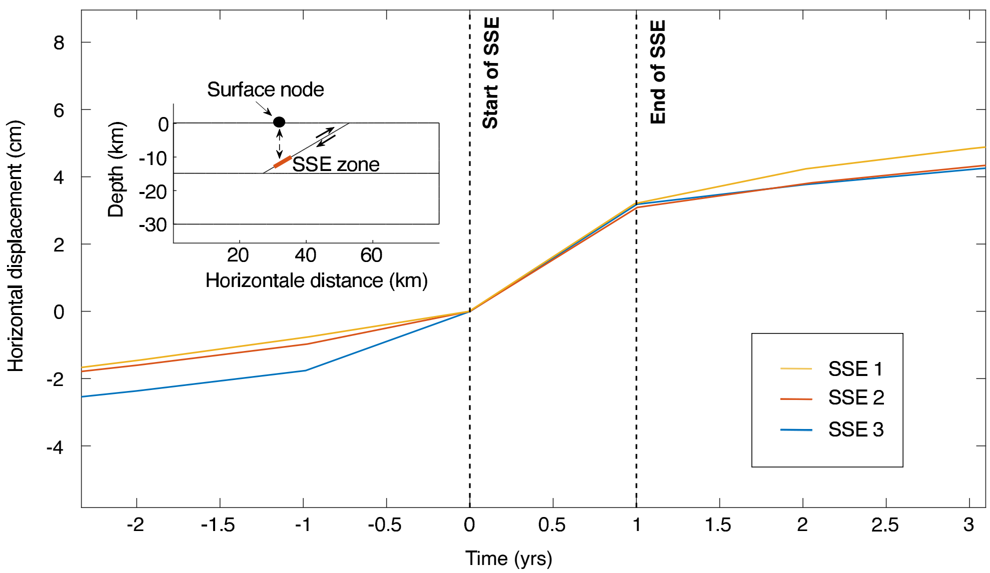

Figure 6. Horizontal displacement recorded at the surface directly above three slow slip events (SSEs) in a simulation with a high fluid production rate (see figure 5c, SSE 1, SSE 2, SSE 3). The time and slip are are both normalised so that they are zero at the onset of each event.

Another interesting feature that we observe in simulations with relatively high rates of interseismic fluid production ($S_0 > 10^{-11}$ s^{-1}) are delayed-slip events, which we also loosely refer to as aftershocks. One such event is illustrated in Figure 7b-d. In this example, a large earthquake is observed to nucleate at approximately 11 km depth that propagates simultaneously downwards to the base of the fault and upward to the surface. Approximately 30 seconds after the nucleation of the large earthquake, a small secondary rupture occurs, which propagates downward with a sliding velocity of about 1 m/s (see figure 7c). Rapid sliding on the fault ceases about 50 seconds after nucleation of the main earthquake. However, about 16 minutes (960 s) after the mainshock, another rupture begins on the upper 5 km of the fault, with sliding rates approaching 0.1 m/s (cf. figure 7a). This delayed slip behavior is directly linked to the coeseismic permeability increase on the fault during the mainshock that allows a fluid pressure pulse to rapidly migrate up and down the fault (see figure 7d), which drives slip on previously ruptured portions of the fault.

The time delay T_D between mainshock and aftershock can be estimated (from the diffusion time scale and equation 5) roughly as

$$T_D \approx \frac{L^2 \eta_f \, \phi \, \beta}{k_{max}} \tag{13}$$

where k_{max} is the coseismic permeability, L the fluid 'diffusion' distance (along the fault),

η_f is the fluid viscosity, ϕ is the porosity and β is the compressibility. For the simulation in Figure 7b T_D is estimated to be approximately 1000 seconds (assuming L=10 km, η_f=1.83x10^{-4} Pa.s, ϕ=0.1, β=5x10^{-10} Pa^{-1} and k_{max} = 10^{-9} m^2), which is of the same order as the observed time between the mainshock and the 'aftershock' (see Figure 8).

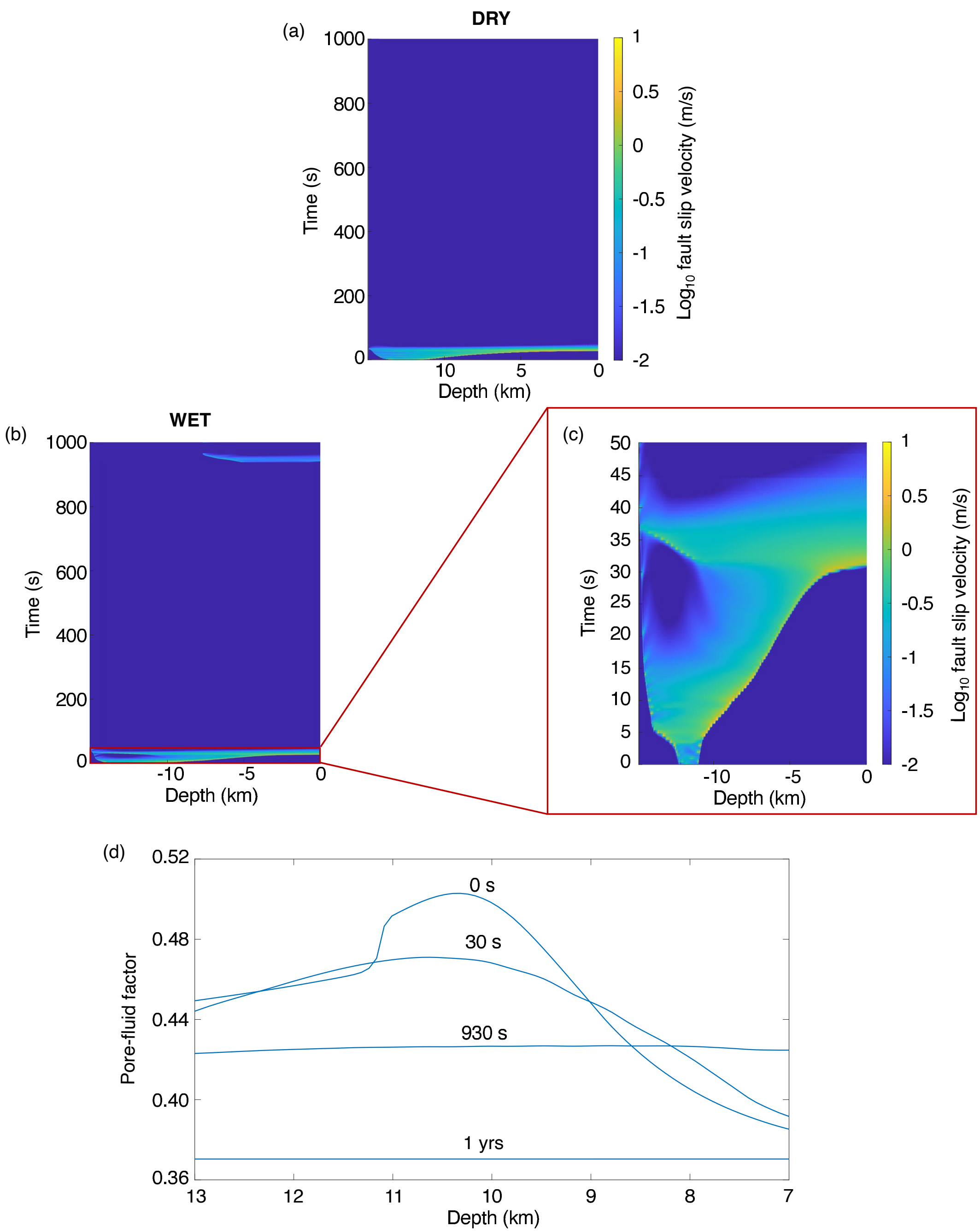

Figure 7. Sliding velocity along the fault during, and in the period shortly after, a large earthquake for a simulation without fluids (a) and with fluids (b, assuming k_{max} = 10^{-9} m^2 and S_0 = 10^{-11} s^{-1}). The panel in (c) shows a zoom to illustrate detail during the main shock. (d), Pore-fluid factor on the fault at the size of maximum fluid production zone (i.e. 10 km depth), at different times after the mainshock nucleation (0s, 30s, 930s and 1 yr). Note the rapid redistribution of fluid overpressures, which is linked to coseismic permeability increase.

This relation suggests that fluid-driven aftershocks are most likely to be distinguishable from mainshocks when fluid transport distances are relatively large and/or when the maximum coseismic permeability is not too high.

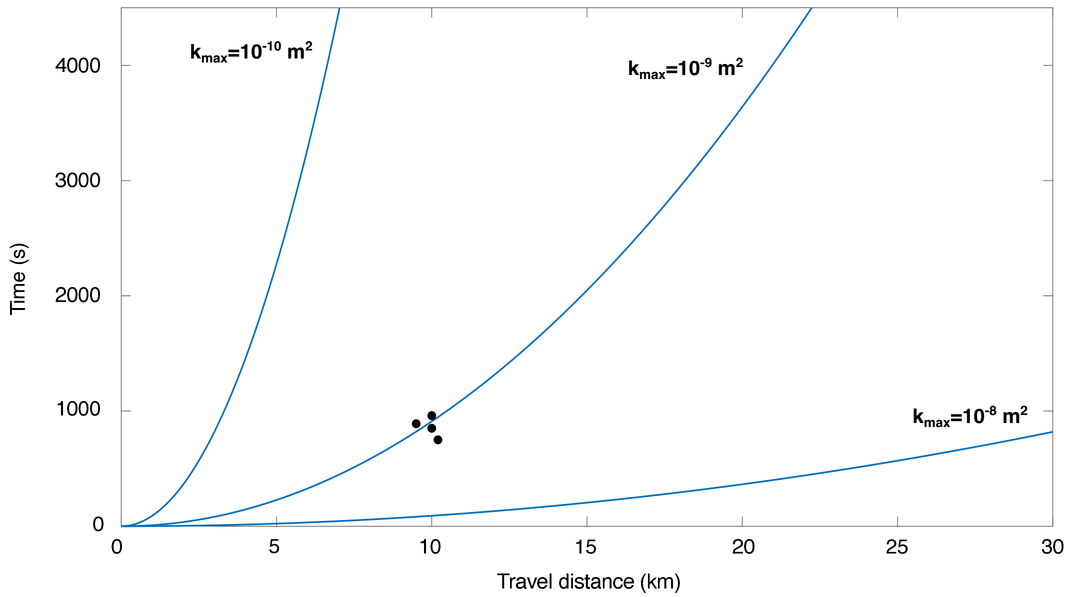

Figure 8. Fluid diffusion time scales versus diffusion length scales (blue curves) for three different coseismic fault permeabilities (see equation 13). Other parameters are listed in Table 1. Black points show durations-distances between mainshocks and aftershocks in simulations with $k_{max} = 10^{-9}$ m^2.

4 Discussion

Our modelling shows that fluids can have both a passive and active influence on earthquakes. The passive effect is due to the influence of fluid pressure in controlling the shear stress at the *onset* of rupture. We predict that if faults are highly overpressured at the time a rupture nucleates, then this will lead to significantly lower coseismic slip, stress drop, slip rates and rupture velocities and a greater tendency for pulse-like rupture propagation than if faults have lower pore pressure states. These aspects are relatively well understood and can be adequately captured by treating the fluid pressure as a tuning parameter, as was done in many previous studies (Lapusta & Rice, 2003; Liu et al., 2005; Kozdon & Dunham, 2013). However, our simulations have shown that fluids can also to play an active role in the earthquake process due to coupled spatiotemporal interactions between fluid and solid deformation, leading to phenomena such as slow slip earthquakes and delayed ruptures. Because neither of these features are observed in our models without fluid, we suggest that they are a fingerprint of fluids involvement in the earthquake process.

In our simulations we observe slow slip events (SSE's) that typically involve about 3 cm of slip at the surface, durations of about 1 year, and peak sliding rates of about 10^{-7} m/s (see Figures 5 and 6). These characteristics are broadly consistent with longer-term SSE's in nature that are sometimes observed close to the downdip limit of the seismogenic zone on thrust faults (Yabe & Ide, 2014; Frank et al., 2015; Obara & Kato, 2016; Wech, 2016; King & Chia, 2018). In nature, SSE's have been observed to precede larger earthquakes by a few months (Radiguet et al., 2016). Our model SSE's also precede larger fast earthquakes, though in simulations the time separation is much longer (about 30 years). The cause of SSE's in nature are unclear but fluids have long been suspected to play a critical role (Warren-Smith et al., 2019; Petrini et al., 2020). Liu and Rice (Liu & Rice, 2005) and Rubin (2008) investigated conditions for SSEs in numerical models based rate- and state-variable friction laws. In these studies, slow slip events are favoured by a low effective normal stresses and/or large slip weakening distances. Although our study is broadly consistent with these results, we show that SSE's can occur at surprisingly high effective stresses (i.e., when the pore pressure is only 55% of the lithostatic pressure). This difference is probably linked to the fact that we have included full poro-elastic coupling. Thus, in our model, pore pressure reduction during initial rupture propagation (induced by volumetric expansion) can act to stabilise the sliding instability, leading to SSE's. Indeed, we observed no SSE's in models where poro-elastic effects were omitted (i.e. term 2 on the right hand side of equation 5, see Figure 9).

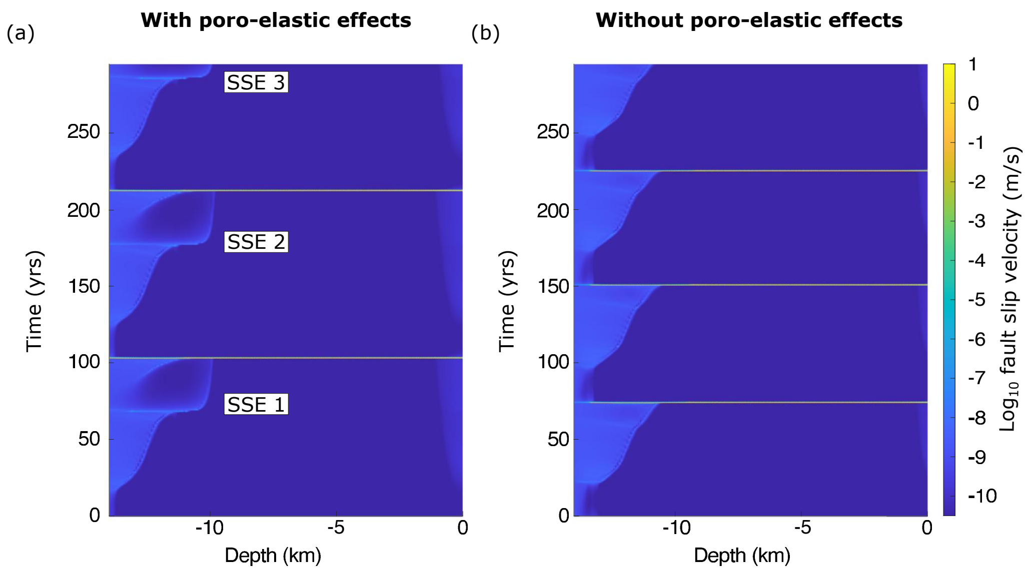

Figure 9. Time depth plots showing the sliding velocity for "wet" simulations ($S_0 = 10^{-10}$ s^{-1}) with (a) and without (b) poro-viscoelastic effects (i.e. pore pressure variation induced by volumetric deformation of the poro-elastic solid). The simulation with the poro-viscoelastic effects shows distinct slow slip events (labeled SSE 1, SSE 2 and SSE 3) in the periods between mainshocks.

Our simulations show that fluid redistribution enabled by an abrupt increase in permeability on the fault during a large rupture (see Fig. 2a) provides a mechanism for generating aftershock-like events. While fluid redistribution is certainly not the only possible cause of aftershocks (Agh-Atabai & Hajati, 2014; Utkucu et al., 2016), the results here are consistent with the modelling studies of Miller et al. (2004), Miller (2020) and Zhu et al. (2020). Miller (2020) suggested that the decay in the rate of aftershocks is controlled by the rate at which a fault (permeability) reseals after a mainshock. In our study we assumed exponential sealing with a characteristic healing time scale T_H of 2 years, which Miller (2020) showed to be broadly consistent with real earthquakes. A healing time scale of 2 years implies that the permeability on the fault recovers only about 2 orders of magnitude in the 10 years following a large earthquake (see Figure 2). In this case, the most important parameter controlling the rate of fluid redistribution is the maximum coseismic permeability k_{max}. Relatively high coseismic permeabilities enable fluid pressure pulses to equilibrate so rapidly that any fluid affects might be indistinguishable from the main rupture. However, lower coseismic permeabilities may lead to a significant delay between mainshock and fluid-driven aftershocks.

Although we find that earthquakes rupturing in the presence of fluid overpressures have quite different characteristics than ruptures in hydrostatically pressured crust, our simulations are not consistent with evidence for extremely weak faults and low stress drops, as discussed in the introduction. In our simulations, fluid pressures never exceed about 60% of the lithostatic stress and shear stresses at the onset of rupture are typically about 90 MPa (see Figure 3d). These stress levels are expected to cause significant shear heating during fast ruptures (Noda et al., 2009). In addition, had we included extreme dynamic weakening (Di Toro et al., 2004; Rice, 2006; Noda et al., 2009; Goldsby & Tullis, 2011), much large stress drops would have occurred. Although we attempted simulations with fluid higher production rates, in order to investigate the influence of higher fluid overpressures these produced unrealistically high uplift rates (even at the surface) due to poro-elastic volumetric expansion in the fluid source zone. This might suggest that fluid sources leading to fluid overpressures in the crust must be laterally localised, possibly limited to the fault zone itself (e.g., see Rice, 1992). Another aspect of our simulations that is somewhat unsatisfactory is that we find rupture velocities ($V_r/C_s < 0.4$) that are significantly lower than found on many continental thrusts (which typically show $V_r/C_s \approx 0.5 - 0.9$) (Huang et al., 2000; Grandin et al., 2015; Chounet et al., 2018; Powali et al., 2020). Once again, we suspect that the rupture velocities in our simulations would be more consistent with observations had we incorporated extreme dynamic weakening at high slip rates due to mechanisms such as thermal pressurization or "flash" heating (Di Toro et al., 2004; Rice, 2006; Noda et al., 2009; Goldsby & Tullis, 2011). We are currently extending our model to include effects such as this.

5 Conclusions

We have developed a model that incorporates rate-and state-dependent sliding on a reverse fault embedded within poro-elastic medium overlying a poro-viscoelastic substrate. Fluid are assumed to be generated in the upper seismogenic layer within a narrow horizontal band lying 10 km below the surface. The permeability is specified to decrease with increasing mean stress, increase dramatically during rapid sliding on the fault and drop exponentially over the interseismic period. The model is compressed from the side to simulate slow tectonic loading. Based on numerical simulations with this model we make the following conclusions:

1. Ruptures occurring in the presence of elevated fluid pressures are characterized by smaller coseismic slip, shear stress drop, peak sliding velocities, rupture velocities and recurrence times compared to models with hydrostatic fluid pressure.
2. In models with relatively high fluid production rates we observed slow slip earthquakes that precede larger and faster earthquakes by approximately 30 years. These slow slip events have durations of about 1 year, sliding rates of about 10^{-7} m/s, and they produce about 3 cm of horizontal displacement at the surface.
3. Some of our models produce delayed slip (resembling aftershocks) that is driven by a fluid pressure pulse travelling up the fault once it ruptures. We find that the delay time between a mainshock and an aftershock scales with the maximum coseismic permeability and the distance over which fluid flow occurs.
4. The influence of fluids on earthquakes in our simulations is due mainly to the modulation of the effective stress and to variations in permeability that control the buidup and dissipation of fluid overpressures. Poroelastic effects are of secondary importance, but are essential for the triggering of slow slip events.
5. Fluids have a noticeable effect on earthquake characteristics and can cause aftershocks and slow slip events even when fluid pressure at the onset of rupture is no more that 60% of the lithostatic stress.

6 Open Research

All the codes and algorithms used to generate and visualise the results discussed in this work are developed with matlab R2020b software. We depend on the "SUITESPARSE" package devoloped by Davis (2006) which is available open access via the following link: `https://github.com/DrTimothyAldenDavis/SuiteSparse/releases`. This package is a suite of sparse matrix algorithms.

Acknowledgments

The Swiss National Science Foundation (project 200021_184626) is thanked for funding. Concerning the AGU data policy, this manuscript is based on results computed from a numerical model and not on data obtained elsewhere by myself or others. The authors declare that they have no conflict of interest.

References

Abercrombie, R. E., & Rice, J. R. (2005). Can observations of earthquake scaling constrain slip weakening? *Geophysical Journal International*, *162*(2), 406–424.

Acosta, M., Passelègue, F., Schubnel, A., & Violay, M. (2018). Dynamic weakening during earthquakes controlled by fluid thermodynamics. *Nature Communications*, *9*(1), 1–9.

Agh-Atabai, M., & Hajati, F. J. (2014). Coulomb stress changes and its correlation with aftershocks of recent Iranian reverse earthquakes. *Arabian Journal of Geosciences*, *8*, 2983-2995.

Allmann, B. P., & Shearer, P. M. (2009). Global variations of stress drop for moderate to large earthquakes. *Journal of Geophysical Research: Solid Earth*, *114*(B1).

Bizzarri, A. (2012). Rupture speed and slip velocity: What can we learn from simulated earthquakes? *Earth and planetary science letters*, *317*, 196–203.

Brace, W., Walsh, J., & Frangos, W. (1968). Permeability of granite under high pressure. *Journal of Geophysical research*, *73*(6), 2225–2236.

Chester, F., & Logan, J. M. (1986). Implications for mechanical properties of brittle faults from observations of the Punchbowl fault zone, California. *Pure and Applied Geophysics*, *124*(1), 79–106.

Chounet, A., Vallée, M., Causse, M., & Courboulex, F. (2018). Global catalog of earthquake rupture velocities shows anticorrelation between stress drop and rupture velocity. *Tectonophysics*, *733*, 148–158.

Connolly, J. (1997). Devolatilization-generated fluid pressure and deformation-propagated fluid flow during prograde regional metamorphism. *Journal of Geophysical Research: Solid Earth*, *102*(B8), 18149–18173.

Cox, S. F. (2005). Coupling between deformation, fluid pressures, and fluid flow in ore-producing hydrothermal systems at depth in the crust. In *One Hundredth Anniversary Volume.* Society of Economic Geologists.

Cox, S. F., & Munroe, S. M. (2016). Breccia formation by particle fluidization in fault zones: implications for transitory, rupture-controlled fluid flow regimes in hydrothermal systems. *American Journal of Science*, *316*(3), 241–278.

Davis, T. A. (2006). *Direct methods for sparse linear systems.* SIAM.

Di Toro, G., Goldsby, D. L., & Tullis, T. E. (2004). Friction falls towards zero in quartz rock as slip velocity approaches seismic rates. *Nature*, *427*(6973), 436–439.

Dieterich, J. H. (1978). Time-dependent friction and the mechanics of stick-slip. In *Rock friction and earthquake prediction* (pp. 790–806). Springer.

Dieterich, J. H. (1979). Modeling of rock friction: 1. experimental results and constitutive equations. *Journal of Geophysical Research: Solid Earth*, *84*(B5), 2161–2168.

Etheridge, M. A., Wall, V., Cox, S., & Vernon, R. (1984). High fluid pressures during regional metamorphism and deformation: implications for mass transport and deformation mechanisms. *Journal of Geophysical Research: Solid Earth*, *89*(B6), 4344–4358.

Evans, J. P., Forster, C. B., & Goddard, J. V. (1997). Permeability of fault-related rocks, and implications for hydraulic structure of fault zones. *Journal of Structural Geology*, *19*(11), 1393–1404.

Fisher, D. M., Brantley, S. L., Everett, M., & Dzvonik, J. (1995). Cyclic fluid flow through a regionally extensive fracture network within the Kodiak accretionary prism. *Journal of Geophysical Research: Solid Earth*, *100*(B7), 12881–12894.

Frank, W. B., Radiguet, M., Rousset, B., Shapiro, N. M., Husker, A. L., Kostoglodov, V., et al. (2015). Uncovering the geodetic signature of silent slip through repeating earthquakes. *Geophysical Research Letters*, *42*(8), 2774–2779.

Goldsby, D. L., & Tullis, T. E. (2011). Flash heating leads to low frictional strength of crustal rocks at earthquake slip rates. *Science*, *334*(6053), 216–218.

Grandin, R., Vallée, M., Satriano, C., Lacassin, R., Klinger, Y., Simoes, M., & Bollinger, L. (2015). Rupture process of the Mw= 7.9 2015 Gorkha earthquake (Nepal): Insights into Himalayan megathrust segmentation. *Geophysical Research Letters*, *42*(20), 8373–8382.

Hedenquist, J. W., & Lowenstern, J. B. (1994). The role of magmas in the formation of hydrothermal ore deposits. *Nature*, *370*(6490), 519–527.

Huang, B.-S., Chen, K.-C., Huang, W.-G., Wang, J.-H., Chang, T.-M., Hwang, R.-D., et al. (2000). Characteristics of strong ground motion across a thrust fault tip from the September 21, 1999, Chi-Chi, Taiwan earthquake. *Geophysical research letters*, *27*(17), 2729–2732.

Im, K., Elsworth, D., & Wang, C. (2019). Cyclic permeability evolution during repose then reactivation of fractures and faults. *Journal of Geophysical Research: Solid Earth*, *124*(5), 4492–4506.

King, C.-Y., & Chia, Y. (2018). Anomalous streamflow and groundwater-level changes before the 1999 M7. 6 Chi–Chi earthquake in Taiwan: possible mechanisms. *Pure and Applied Geophysics*, *175*(7), 2435–2444.

Kozdon, J. E., & Dunham, E. M. (2013). Rupture to the trench: Dynamic rupture simulations of the 11 March 2011 Tohoku earthquake. *Bulletin of the Seismological Society of America*, *103*(2B), 1275–1289.

Lapusta, N., & Rice, J. R. (2003). Nucleation and early seismic propagation of small and large events in a crustal earthquake model. *Journal of Geophysical Research: Solid Earth*, *108*(B4).

Leclère, H., Faulkner, D., Llana-Fúnez, S., Bedford, J., & Wheeler, J. (2018). Reaction fronts, permeability and fluid pressure development during dehydration reactions. *Earth and Planetary Science Letters*, *496*, 227–237.

Liu, S.-F., Nummedal, D., Yin, P.-G., & Luo, H.-J. (2005). Linkage of Sevier thrusting episodes and Late Cretaceous foreland basin megasequences across southern Wyoming (USA). *Basin Research*, *17*(4), 487–506.

Liu, Y., & Rice, J. R. (2005). Aseismic slip transients emerge spontaneously in three-dimensional rate and state modeling of subduction earthquake sequences. *Journal of Geophysical Research: Solid Earth*, *110*(B8).

Manning, C., & Ingebritsen, S. (1999). Permeability of the continental crust: Implications of geothermal data and metamorphic systems. *Reviews of Geophysics*, *37*(1), 127–150.

Marone, C. (1998). The effect of loading rate on static friction and the rate of fault healing during the earthquake cycle. *Nature*, *391*(6662), 69–72.

Miller, S. A. (1997). *The behavior of 3-dimensional fluid-controlled earthquake model: applications and implications* (Unpublished doctoral dissertation). ETH Zurich.

Miller, S. A. (2020). Aftershocks are fluid-driven and decay rates controlled by permeability dynamics. *Nature Communications*, *11*(1), 1–11.

Miller, S. A., Collettini, C., Chiaraluce, L., Cocco, M., Barchi, M., & Kaus, B. J. (2004). Aftershocks driven by a high-pressure CO_2 source at depth. *Nature*, *427*(6976), 724–727.

Miller, S. A., & Nur, A. (2000). Permeability as a toggle switch in fluid-controlled crustal processes. *Earth and Planetary Science Letters*, *183*(1-2), 133–146.

Noda, H., Dunham, E. M., & Rice, J. R. (2009). Earthquake ruptures with thermal weakening and the operation of major faults at low overall stress levels. *Journal of Geophysical Research: Solid Earth*, *114*(B7).

Noda, H., Lapusta, N., & Rice, J. R. (2011). Earthquake sequence calculations with dynamic weakening mechanisms. In *Multiscale and multiphysics processes in geomechanics* (pp. 149–152). Springer.

Obara, K., & Kato, A. (2016). Connecting slow earthquakes to huge earthquakes. *Science*, *353*(6296), 253–257.

Osborne, M. J., & Swarbrick, R. E. (1998). Mechanisms for generating overpressure in sedimentary basins: a reevaluation. *AAPG Bulletin*, *82*(12), 2270–2271.

Passelègue, F. X., Almakari, M., Dublanchet, P., Barras, F., Fortin, J., & Violay, M. (2020). Initial effective stress controls the nature of earthquakes. *Nature Communications*, *11*(1), 1–8.

Petrini, C., Gerya, T., Yarushina, V., van Dinther, Y., Connolly, J., & Madonna, C. (2020). Seismo-hydro-mechanical modelling of the seismic cycle: Methodology and implications for subduction zone seismicity. *Tectonophysics*, *791*, 228504.

Powali, D., Sharma, S., Mandal, R., & Mitra, S. (2020). A reappraisal of the 2005 Kashmir (Mw 7.6) earthquake and its aftershocks: Seismotectonics of NW Himalaya. *Tectonophysics*, *789*, 228501.

Radiguet, M., Perfettini, H., Cotte, N., Gualandi, A., Valette, B., Kostoglodov, V., et al. (2016). Triggering of the 2014 Mw7. 3 Papanoa earthquake by a slow slip event in Guerrero, Mexico. *Nature Geoscience*, *9*(11), 829–833.

Renard, F., Gratier, J.-P., & Jamtveit, B. (2000). Kinetics of crack-sealing, intergranular pressure solution, and compaction around active faults. *Journal of Structural Geology*, *22*(10), 1395–1407.

Rice, J. R. (1992). Fault stress states, pore pressure distributions, and the weakness of the San Andreas fault. , *51*, 475–503.

Rice, J. R. (2006). Heating and weakening of faults during earthquake slip. *Journal of Geophysical Research: Solid Earth*, *111*(B5).

Rubin, A. M. (2008). Episodic slow slip events and rate-and-state friction. *Journal of Geophysical Research: Solid Earth*, *113*(B11).

Ruina, A. (1983). Slip instability and state variable friction laws. *Journal of Geophysical Research: Solid Earth*, *88*(B12), 10359–10370.

Scholz, C. H. (1998). Earthquakes and friction laws. *Nature*, *391*(6662), 37–42.

Scholz, C. H. (2006). The strength of the San Andreas fault: A critical analysis. *Geophysical Monograph Series*, *170*, 301.

Selvadurai, A., Boulon, M., & Nguyen, T. (2005). The permeability of an intact granite. *Pure and Applied Geophysics*, *162*(2), 373–407.

Sibson, R. H. (1986). Rupture interaction with fault jogs. *Earthquake Source Mechanics*, *37*, 157–167.

Sibson, R. H. (1990). Conditions for fault-valve behaviour. *Geological Society, London, Special Publications*, *54*(1), 15–28.

Sibson, R. H. (1992). Implications of fault-valve behaviour for rupture nucleation and recurrence. *Tectonophysics*, *211*(1-4), 283–293.

Sibson, R. H. (2017). Tensile overpressure compartments on low-angle thrust faults. *Earth, Planets and Space*, *69*(1), 1–15.

Sibson, R. H., Robert, F., & Poulsen, K. H. (1988). High-angle reverse faults, fluid-pressure cycling, and mesothermal gold-quartz deposits. *Geology*, *16*(6), 551–555.

Simpson, G. (2017). *Practical finite element modeling in earth science using matlab.* John Wiley & Sons.

Simpson, G. (2018). What do earthquakes reveal about ambient shear stresses in the upper crust? *Geology*, *46*(8), 703–706.

Sleep, N. H., & Blanpied, M. L. (1992). Creep, compaction and the weak rheology of major faults. *Nature*, *359*(6397), 687–692.
Suppe, J. (2014). Fluid overpressures and strength of the sedimentary upper crust. *Journal of Structural Geology*, *69*, 481–492.
Tenthorey, E., Cox, S. F., & Todd, H. F. (2003). Evolution of strength recovery and permeability during fluid–rock reaction in experimental fault zones. *Earth and Planetary Science Letters*, *206*(1-2), 161–172.
Tsutsumi, A., & Shimamoto, T. (1997). High-velocity frictional properties of gabbro. *Geophysical Research Letters*, *24*(6), 699–702.
Utkucu, M., Durmuş, H., & Nalbant, S. S. (2016). Stress history controls the spatial pattern of aftershocks: case studies from strike-slip earthquakes. *International Journal of Earth Sciences*, *106*, 1841-1861.
Walder, J., & Nur, A. (1984). Porosity reduction and crustal pore pressure development. *Journal of Geophysical Research: Solid Earth*, *89*(B13), 11539–11548.
Warren-Smith, E., Fry, B., Wallace, L., Chon, E., Henrys, S., Sheehan, A., et al. (2019). Episodic stress and fluid pressure cycling in subducting oceanic crust during slow slip. *Nature Geoscience*, *12*(6), 475–481.
Wech, A. G. (2016). Extending Alaska's plate boundary: Tectonic tremor generated by Yakutat subduction. *Geology*, *44*(7), 587–590.
Weis, P., Driesner, T., & Heinrich, C. A. (2012). Porphyry-copper ore shells form at stable pressure-temperature fronts within dynamic fluid plumes. *Science*, *338*(6114), 1613–1616.
Xue, L., Li, H.-B., Brodsky, E. E., Xu, Z.-Q., Kano, Y., Wang, H., et al. (2013). Continuous permeability measurements record healing inside the Wenchuan earthquake fault zone. *Science*, *340*(6140), 1555–1559.
Yabe, S., & Ide, S. (2014). Spatial distribution of seismic energy rate of tectonic tremors in subduction zones. *Journal of Geophysical Research: Solid Earth*, *119*(11), 8171–8185.
Zheng, G., & Rice, J. R. (1998). Conditions under which velocity-weakening friction allows a self-healing versus a cracklike mode of rupture. *Bulletin of the Seismological Society of America*, *88*(6), 1466–1483.
Zhu, W., Allison, K. L., Dunham, E. M., & Yang, Y. (2020). Fault valving and pore pressure evolution in simulations of earthquake sequences and aseismic slip. *Nature Communications*, *11*(1), 1–11.